Steep gravity–capillary waves within the internal resonance regime

Marc Perlin and Chao-lung Ting
Department of Naval Architecture and Marine Engineering, University of Michigan, Ann Arbor, Michigan 48109

(Received 14 February 1992; accepted 26 June 1992)

Steep gravity–capillary waves are studied experimentally in a channel. The range of cyclic frequencies investigated is 6.94–9.80 Hz; namely, the high-frequency portion of the regime of internal resonances according to the weakly nonlinear theory (Wilton's ripples). These wave trains are stable according to the nonlinear Schrödinger equation. The experimental wave trains are generated by large, sinusoidal oscillations of the wavemaker. A comparison is made between the measured wave fields and the (symmetric) numerical solutions of Schwartz and Vanden-Broeck [J. Fluid Mech. **95**, 119 (1979)], Chen and Saffman [Stud. Appl. Math. **60**, 183 (1979); **62**, 95 (1980)], and Huh (Ph.D. dissertation, University of Michigan, 1991). The waves are shown to be of slightly varying asymmetry as they propagate downstream. Their symmetric parts, isolated by determining the phase which provides the smallest mean-square antisymmetric part, compare favorably with the "gravity-type" wave solutions determined by numerical computations. The antisymmetric part of the wave profile is always less than 30% of the peak-to-peak height of the symmetric part. As nonlinearity is increased, the amplitudes of the short-wave undulations in the trough of the primary wave increase; however, there are no significant changes in these short-wave frequencies. The lowest frequency primary-wave experiments, which generate the highest frequency short-wave undulations, exhibit more rapid viscous decay of these high-frequency waves than do the higher-frequency primary wave experiments.

I. INTRODUCTION

Since the advent of multiple-scales perturbation techniques as well as averaged-Lagrangian techniques to investigate weakly nonlinear resonant interactions of waves, there has been significant progress in understanding weakly nonlinear gravity–capillary (GC) waves. For a relatively complete literature review, see Perlin and Hammack.[1] Numerical investigations of strongly nonlinear, inviscid GC waves with assumed symmetry about the crest and/or trough have been conducted by Schwartz and Vanden-Broeck,[2] Chen and Saffman,[3–5] and more recently by Huh.[6] Schwartz and Vanden-Broeck investigated two-dimensional waves using a boundary-integral formulation/Newton iteration and found multiple solutions that exhibit multipeaked crests and troughs. Concurrently, Chen and Saffman also investigated permanent form GC waves on deep water. They reexamined the weakly nonlinear problem of Wilton's ripples[3] and demonstrated that they are a special case of a general bifurcation. In a follow-up investigation,[4] they examined finite-amplitude waves using the Stokes expansion with Newton iteration. In a subsequent investigation,[5] they addressed the problem in three dimensions. Huh reproduced previous two-dimensional results using a spectral boundary-integral formulation and was able to show numerically that certain of these results are unstable. That is, they used the periodicity condition to obtain highly accurate solutions and then removed the temporal periodicity constraint.

Experimental investigations include those of Schooley[7] who investigated wind-generated, multidimpled 9.8 Hz waves; however, the authors are unaware of any systematic experimental studies of waves in the internal resonance regime, the subject of the present effort.

Herein, steep GC waves are generated mechanically in a channel and the results are compared to the aforementioned computations. To retain two-dimensionality of the wave field in the experiments, the wavemaker stroke is limited. An understanding of these small-scale waves is required to more accurately predict surface roughness which significantly impacts, for example, radar backscatter from sea surfaces. The purpose of this research is to compare numerical predictions with experimental results. In Sec. II, the numerical method used by Schwartz and Vanden-Broeck is discussed and pertinent results from the references cited above are presented. In Sec. III, there is a discussion of the laboratory facility as well as data analysis techniques. Section IV presents the results of the comparison between theory and experiments, while Sec. V offers conclusions.

II. NUMERICAL SOLUTIONS

A condensed version of the numerical treatment of the exact, two-dimensional water wave problem including surface tension and gravity as afforded by Schwartz and Vanden-Broeck is presented. Following their analysis, two-dimensionality and an infinite depth fluid which is inviscid, incompressible, and of constant density is assumed. Further, the assumption of irrotational flow is required. The waves are assumed of permanent form and symmetric about a vertical axis at both the crest and trough. Thus, computations are only carried out for half of the wave-form. Under these assumptions, a complex physical coor-

 0899-8213/92/112466-13$04.00

dinate, $z=x+iy$, a complex potential, $f(z)=\phi+i\psi$, and a complex velocity, $q=df/dz=u-iv$, are defined. In coordinates moving at the constant phase speed, c, the kinematic condition is identically satisfied while the dynamic condition on the free surface is

$$\frac{1}{2}qq^*+gy+\frac{T}{\rho R}=\frac{1}{2}c^2, \tag{1}$$

where g is the acceleration of gravity, T is the surface tension, ρ is the mass density, and R is the surface radius of curvature with positive defined with center in the fluid. Three dimensionless parameters are chosen as follows: the dimensionless surface-tension parameter (following Wilton's original work), $\kappa=(k^2T)/(\rho g)$; the dimensionless wave-speed parameter, $\mu=(k/g)c^2$; and a dimensionless measure of wave steepness, $\epsilon=[y(0)-y(\pi/k)]/[(2\pi)/k]$, whose choice is unclear for multicrested steep waves. Here k is the wave number; $\kappa=1/n$ represents the nth-harmonic resonance for the weakly nonlinear theory. Using the first two dimensionless parameters, Eq. (1) becomes

$$\frac{1}{2}\hat{q}\hat{q}^*+\hat{y}+\frac{\kappa}{\hat{R}}=\frac{1}{2}\mu, \tag{2}$$

where the circumflexes denote dimensionless variables. Next the flow is separated into a uniform part and a wave part using the transformation $\hat{z}=\mu^{-1/2}\hat{f}+\hat{\mathbf{z}}$. Periodicity is imposed using the mapping $\hat{f}=\hat{\phi}+i\hat{\psi}=i\mu^{1/2}\log\zeta$, where $\zeta=re^{i\theta}$ and $r=1$ is the surface. Schwartz and Vanden-Broeck, after exploiting the assumed symmetry of the permanent-form wave, expressed the surface condition in terms of the unknown function, $\hat{z}=\hat{z}[\hat{x}(\theta),\hat{y}(\theta)]$, as

$$\frac{\hat{y}}{\mu}+\frac{1}{2}\left(\frac{1}{\hat{x}'^2+\hat{y}'^2}-1\right)+\frac{\kappa}{\mu}\left(\frac{\hat{x}'\hat{y}''-\hat{y}'\hat{x}''}{(\hat{x}'^2+\hat{y}'^2)^{3/2}}\right)=0, \tag{3}$$

where the primes denote differentiation with respect to θ. They chose to fix (κ,ϵ) and vary μ. A Newton–Raphson technique was used to solve the set of nonlinear algebraic equations obtained by finite differencing (3).

Multiple solutions are found. That is, for given values of (κ,ϵ), several numerical solutions are found with different values of the speed parameter μ. Their Fig. 8 is reproduced here as Fig. 1 for reference. As nondimensionalized by Schwartz and Vanden-Broeck, the wavelength was 2π, and since it was assumed symmetric about π, only half of the waveforms need be shown. The ordinate is y. Figure 1 shows the four solutions calculated for $\kappa=0.33$. Reference will be made to waves of this general type. Waveforms of type-3 were termed "gravity dominant" (or gravity-type) because, in the limiting case of no high-frequency perturbations, the waveform has wide troughs and narrow crests as does a steep gravity wave, while waveforms of type-1 were termed "capillary dominant" (or capillary-type) because of their wide crests and narrow troughs.

As mentioned previously, Chen and Saffman[4] also calculated wave profiles for steep, two-dimensional GC waves (using a different technique). Their Fig. 10 is included as Fig. 2 as waves of these general forms are found experimentally. Clearly, as primary-wave steepness increases,

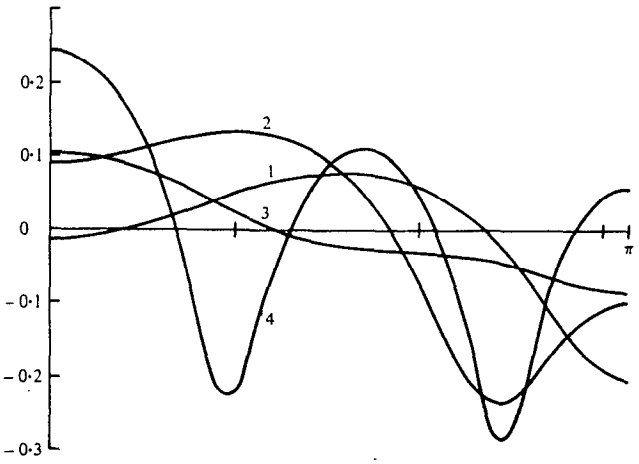

FIG. 1. Numerically computed wave profiles of Schwartz and Vanden-Broeck for $\kappa=0.33$. (Courtesy of J. Fluid Mech.)

shorter waves form along the entire primary wave, and eventually become steeper in the primary-wave trough, less steep in the primary-wave crest. (Presumably, one can argue that the shorter waves are stretched by the primary wave in the crest region and compressed in the trough region due to the effects of the long-wave current on the shorter waves.) Also, note that for the steepest case, bubbles are pinched off in the crests as predicted by the exact theory of Crapper[8] for a single capillary wave. A discussion of these nonlinear waveforms is given in Sec. IV.

III. LABORATORY FACILITY AND DATA ANALYSIS

The laboratory facility consists of five subsystems: wave tank; wavemaker and attendant electronics; wavemaker signal generation and data acquisition system; wave gauges and attendant electronics; and water treatment system. Glass walls, separated 30.5 cm, form a 130 cm channel downstream of the wavemaker. The water depth is approximately 15 cm (deep water according to the linear wave theory for the frequencies reported). The wavemaker consists of an Unholtz-Dickie electrodynamic shaker Model 20 with a model TA100-20 amplifier; an aluminum right-angle-wedge wave paddle; and a feedback displacement transducer, Kaman model KD2300-10CU. The paddle dimensions are 2.71 cm vertical by 1.32 cm horizontal with a downstream face angled 26° from the vertical. Under static conditions, the wave paddle is immersed about 1.35 cm. The command signal (shaker digital-to-analog signal) is generated at 3000 Hz and data acquisition is accomplished using a Mac IIfx computer enhanced by National Instruments' LabVIEW software and data acquisition hardware packages. Capacitance-type wave probes are used with an outside diameter of only 0.5 mm to minimize its disturbance. (Dynamic calibration of the wave probes demonstrated a resolution of ~0.03 mm.) Prior to digitization, output as well as input signals are filtered using two Krohn-Hite model 3342 analog filters with a cutoff frequency of 250 Hz. These signals are monitored to ensure that the actual signal is essentially the same as the desired

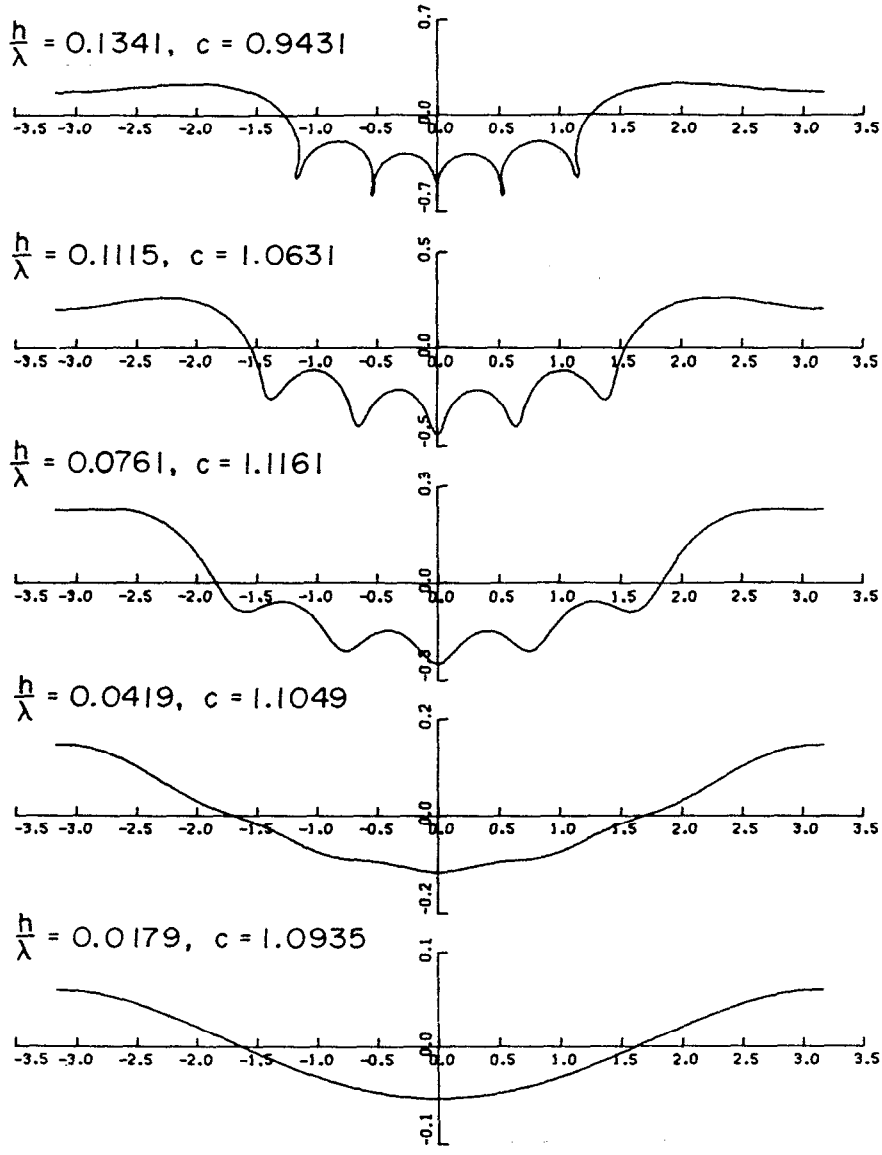

FIG. 2. Profiles as found by Chen and Saffman for varying steepnesses with $\kappa=0.19$. (Courtesy of Stud. Appl. Math.)

signal. The water treatment system includes a 5 mm particulate prefilter, double deionization tanks, a carbon adsorption phase, and a 0.2 mm particulate final filter. The wave tank and paddle are scrubbed meticulously before and after each use with ethyl alcohol. Static surface-tension measurements using a CSC-DuNoüy tensiometer are made routinely and agree with those of clean water at room temperature; however, it is well known that the presence of surface-active agents does not necessarily cause a significant change in static surface-tension measurements. Thus, the presence of these contaminants cannot be entirely ruled out.

Following low-pass filtering at 250 Hz, wave gauge data are digitized at 500 Hz with a record length of 2^{13} samples which generate time series with a resolution of 0.061 Hz. Approximately 10 mV of broadband noise contaminates the record, and is manifested in the high-frequency regime once the transfer function is applied due to the increase in the transfer function with frequency. [The transfer function is determined dynamically by attaching the wave probe to the shaker and making a frequency-by-frequency comparison of output displacement (from the displacement-feedback transducer) and wave-probe voltage.] To circumvent the noise-contamination problem, the following technique is used. Upon demonstrating temporal periodicity of the wave field at a particular spatial location (which is the case for all the experiments presented), the output-frequency signal to the shaker is altered slightly from the desired frequency, for each set of experiments, so that an integral number of data points exist for each period of the generated wave. Then, the time series is divided into an integral number of waves with a partial wave discounted. This set, consisting of an integral number of waves plus their corresponding broad-

TABLE I. Summary of time-averaging parameters.

Experimental frequency (Hz)	Dimensionless surface tension, κ	Number of points per wave, N	Integral number of waves per record
9.80	1/2	51	160
8.93	1/2.5	56	146
8.33	1/3	60	136
7.94	1/3.5	63	130
7.58	1/4	66	124
7.25	1/4.5	69	118
6.94	1/5	72	113

band noise, is averaged to obtain one averaged-wave period. This technique reduces broadband noise in a periodic signal at all frequencies except the superharmonics. These remaining frequencies have insufficient amplitudes to contaminate the waveform in a visible manner (even after the transfer function is applied as discussed below) for the signal-to-noise ratios present in the experiments. Test cases demonstrated that the method works well for signal-to-noise ratios as low as 10, which is less than the lowest ratio in the experiments. Further supporting evidence of the success of this method is seen in the experiments, especially with small ka values. (For example, see Fig. 7. The smallest ka value in the experiments, $ka=0.013$, has a measured waveform with no spurious, high-frequency undulations present.)

The time series is reconstructed by using the averaged waveform repeatedly as required until 2^{13} data points are obtained. This time series is then Fourier transformed, the transfer function of the wave probe is applied with a high-frequency cutoff of 55 Hz, and the resulting amplitude spectrum is inverse Fourier transformed to obtain the final profiles of surface elevation versus time. As the mean has been subtracted, $y=0$ is the mean water level. Table I presents a summary of the parameters used in the time-averaging procedure for each experimental frequency presented in Sec. IV. (Because of the large number of waves in each time series, neglect of a partial wave even without windowing, does not affect the results appreciably, especially since the higher frequencies are filtered.) An alternate approach is to use the data directly from the wave probe without the transfer function and the cutoff frequency. Since the attenuation of the wave probe is essentially a low-pass filter (to approximately 50 to 60 Hz), this alternate approach yields nearly identical data for the first six to eight harmonics throughout the range of frequencies reported.

The decomposition of a waveform into its symmetric and antisymmetric parts is described next. It is used in Sec. IV. The number of points per wave, N, is presented in Table I. If $y(i)$ is defined as the fluid-surface elevation at the ith point in a time series one wave period (N points) in duration, and M is the point for which the symmetric and antisymmetric parts are computed, then

$$[y_{\mathrm{sym}}(j)]_M=\frac{y(j)+y(-j)}{2},$$
$$[y_{\mathrm{antisym}}(j)]_M=\frac{y(j)-y(-j)}{2},\qquad i=1,N,$$

where

$$\pm j=\begin{Bmatrix} M\pm i+N, & \text{if} & (M\pm i)<1 \\ M\pm i, & \text{if} & 1\leqslant(M\pm i)\leqslant N \\ M\pm i-N, & \text{if} & (M\pm i)>N \end{Bmatrix},\quad i=1,N. \tag{4}$$

The mean-square difference between the measured profile and the symmetric part calculated above for each of N values of M is computed as follows:

$$\epsilon_M=\frac{1}{N}\sum_{j=1}^{N}[y_{\mathrm{meas}}(j)-y_{\mathrm{sym}}(j)]^2. \tag{5}$$

The data point with the smallest mean-square difference between the original waveform and the computed symmetric part, ϵ_M, is chosen as the data point of symmetry.

IV. RESULTS

The objectives of the experiments are an increased understanding of steep GC waves and a comparison to numerical predictions. There are, however, two fundamental differences between the experiments and the computations. The experiments are periodic in time and spatially varying while the numerics are assumed periodic in space. Nothing is done to rectify this difference. Also, viscous effects are present in the physical experiments.

In the seven sets of experiments, surface profiles are recorded three, four, and five wavelengths (where the wavelength λ is computed from periodic linear theory) downstream of the wavemaker, except for the 9.80 Hz experiments which are recorded at four, five, and six wavelengths downstream. In addition, none of the experiments are three dimensional (i.e., the wavemaker-stroke amplitude, s, is limited such that the wave field is two dimensional). The wavemaker is oscillated at the corresponding experiment's single frequency, only.

A. The 9.80 Hz experiments

In Fig. 3, waveforms are presented for five values of wavemaker-stroke steepness (defined as the product of the wave number k and the stroke amplitude s) at three downstream locations for the 9.80 Hz experiments corresponding to $\kappa=1/2$. On each time series, the wave steepness [defined as the product of the wave number k and the amplitude a, with a defined as $(y_{\max}-y_{\min})/2$] is shown. Also shown, in the second and third rows of this figure, are the symmetric and antisymmetric parts of the largest wavemaker-steepness, 9.80 Hz experiment which is discussed below. For each plot, the abscissas are wave elevation in mm and the ordinates are time in msec. The wave-

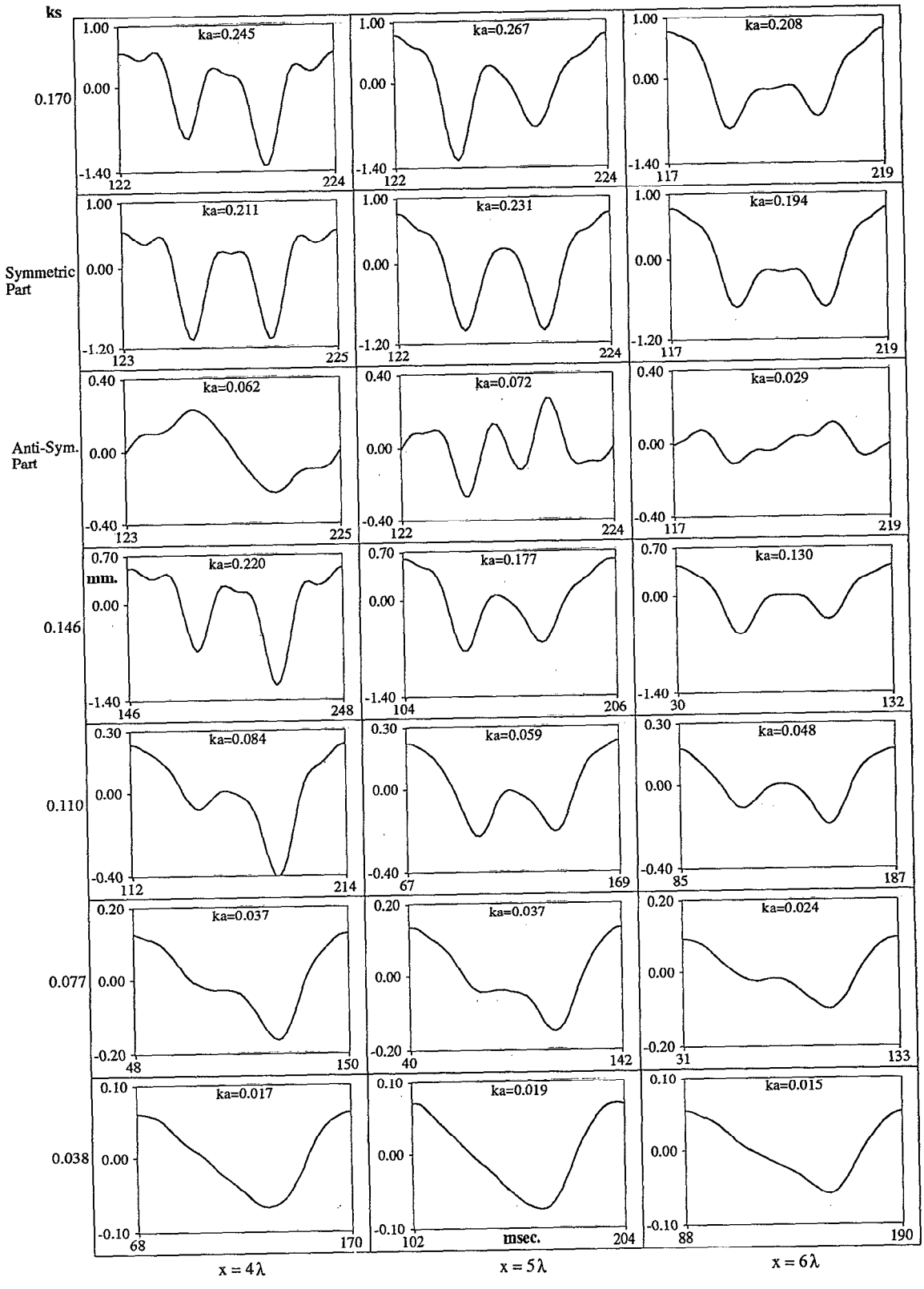

FIG. 3. Wave profiles from the 9.80 Hz experiments are shown for three downstream locations as a function of wavemaker steepness. In addition, the wave profiles from the largest wavemaker steepness are shown decomposed into their symmetric and antisymmetric parts.

forms are presented with the maximum elevations as the (arbitrary) starting points. One period of each waveform is shown.

It is immediately apparent in Fig. 3 that the primary wave and its second harmonic are phase locked, and, that the waveform is asymmetric in time as well as in space. The asymmetry is discussed below. The phasing between the first and second harmonic remains approximately constant such that, at larger ka, the primary crest and primary trough both occur with a secondary crest. As the wavemaker-stroke steepness ks is increased (a measure of nonlinearity of the system), so is the magnitude of the second harmonic. Also, note the similarity between the profiles of $ks=0.146$ and 0.170. Although the stroke of the paddle is restricted to maintain two-dimensionality (as determined by a visual check) and the filter cutoff frequency of 55 Hz precludes the measurement of profiles with very steep slopes, the waves are in the *strongly* nonlinear regime (i.e., the waves are not simply a superposition of linear waves that exchange energy through resonant interaction at the second order). As further evidence of the strongly nonlinear nature of these experiments, note that the elapsed time between successive troughs in the first experiment is 37 msec. If the second harmonic was a free linear wave train, this time would be 51 msec. Note, further, that the elapsed time between successive troughs does not increase as the steepness decreases downstream (due to viscosity) nor as the steepness decreases due to a decrease in wavemaker stroke; however, a decreasing second-harmonic magnitude (relative to the primary harmonic) is measured as ks is decreased. One further note is that the waveforms for $ks=0.077$ show reasonable qualitative agreement with the results of McGoldrick (Fig. 9).[9]

Using the definition of "type number" as given by Schwartz and Vanden-Broeck[2] as indicative of the number of dimples or inflection points on a half-waveform, it is seen that most of the 9.80 Hz waves are type-2 (or so-called "gravity-type") profiles with a second-harmonic crest very evident in the trough of the primary harmonic. Nearest the wavemaker, the two most nonlinear experiments have additional dimples on the crests of the primary and secondary waves. With the exception of the smallest wavemaker-stroke steepness, all profiles exhibit the type-2 waveform. In fact, all waveforms seen here exhibit gravity-type profiles.

Another feature of the steepest waveforms shown in Fig. 3, which is similar to the very steep waves shown in Fig. 2, is the increase in short-wave amplitude in the primary-wave trough which is accompanied by a narrowing of the two troughs to either side of the second-harmonic crest (which precedes bubble encapsulation in the numerical solutions). These second-harmonic waves are thus shaped like capillary waves. Physically, one may argue as do Schwartz and Vanden-Broeck that the short-wave train (second harmonic) is riding on a primary wave (first harmonic) which the short wave "sees" as a current. Thus, there is a stretching of the short wave on the crest of the primary wave where the short wave is traveling on a following current and a steepening of the short wave in the trough of the primary wave where the short wave is traveling on an opposing current. This argument has been advanced by others in connection with long-wave/short-wave interaction, for example, see Phillips.[10] Regarding bubble encapsulation as predicted by Crapper's exact (two-dimensional) solution and the numerical solutions discussed, experimental results suggest that for waves generated mechanically in a wide channel, three-dimensional instabilities preclude bubble formation. (Recall that the wavemaker stroke is limited such that only two-dimensional wave fields result. In results not reported, increased stroke generates three-dimensional wave fields with reduced wave steepnesses.) This is aside from whether viscous effects preclude their formation or whether a narrow channel (on the order of less than a wavelength) would facilitate their formation. Narrow channels are known to cause interesting effects.[11]

Although the amplitude of the higher-frequency wave is increased, and a narrowing of its troughs is accompanied by a widening of its crest, there is no noticeable change in its frequency. This is in contradiction to the theory as is seen from Fig. 2 where the undulations are more concentrated in a shorter, primary-wave trough.

Another interesting feature seen in the numerically computed waveforms and discussed by Schwartz and Vanden-Broeck is the inclination with respect to the vertical of the troughs of the short waves (other than the one located at midtrough of the primary wave) which eventually encapsulate bubbles. This is shown clearly in the steepest profile of Fig. 2. Evidence of this is not seen in the experimental data. Possible reasons include insufficient steepness (precluded by evolution to three dimensions and thus not investigated), the data analysis technique, disturbances due to the use of *in situ* wave probes, and, of course, that physically it does not occur.

Aside from the $ks=0.170$ experiment, the upstream face of the primary wave has a smaller slope, on average, than does the downstream face. This is seen readily in the $ks=0.038$ experiment; however, it is in accordance with all of the experiments presented. One explanation of the difference between upstream-face slope and downstream-face slope is that there is a finite time required during which fluid drains from the wave probe as the water surface falls, thus causing a reduced slope in the measurement of the upstream face. This effect is not present as the surface rises. Recent measurements in our laboratory have shown that this is not the case and that the asymmetry exists in both time and space. (An optical technique has been developed which enables measurement of a time series of spatial profiles. This technique, as well as spatial surface profiles will be the subject of a future paper. At the time the present work was conducted, the instrumentation required to make these measurements was unavailable to us.) Spatial images, as well as time series of surface elevation at a given location (which correspond to the wave-probe time series presented), show that the forward face is steeper than the leeward face. In fact, the agreement between the wave-probe generated time series and the optical-system generated time series is remarkable.

Finally, it is remarked that the wave steepness ka may actually increase as viscosity dampens the wave in the downstream direction. This is shown, for example, in the $ks=0.170$ experiment. At five wavelengths downstream, the wave steepness is larger than it is at four wavelengths downstream. The second harmonic, however, has diminished in size in the downstream direction. Thus, as discussed by the numericists, wave steepness is not a good descriptor for these nonlinear, multipeaked waveforms.

To investigate the asymmetry in the wave profiles, the waveform is decomposed into its symmetric and antisymmetric parts as described in Sec. III. The purpose of this decomposition is to compare the symmetric part of the experimentally measured profile with the computed waveforms, assumed symmetric at the outset, and to determine the cause of the asymmetry. In Fig. 3, the results of this decomposition is shown for the largest wavemaker stroke of the 9.80 Hz experiment. The symmetry point with the least mean-square antisymmetric part is within 2% of a temporal period from the midpoint between the global maximum of the waveform. This is shown by the difference between the initial point of the waveform and the initial points of the symmetric and antisymmetric profiles. In all three columns, the symmetric part is qualitatively similar to the type-2 waves as discussed previously. It is hoped that the antisymmetric part is also a recognizable waveform, perhaps one of the numerical solutions with a different phase than that of the symmetric part. That is, does a nonlinear superposition of wave trains exist with differing phase speeds which thus produce the varying asymmetry? The answer to this question is no; however, some observations are made regarding the antisymmetric part of the waveforms. One additional attempt is made to investigate the antisymmetric part by repeating the above decomposition on it. This produces reasonable waveforms that are comparable to the various numerical solutions; however, these waveforms are not of permanent form as they propagate downstream. Thus, this latter decomposition is abandoned.

The use of antisymmetric waveforms is an artifice. It is used in an attempt to explain the asymmetry of the nonlinear wave trains. Although apparently not proven for GC waves, it is reasonable to expect a wave of permanent form to possess symmetry. The experimental wave trains are not symmetric, but are recognizably similar downstream. The 9.80 Hz decomposition shown in Fig. 3 reinforces that the general, overall shape of the profiles agree with the computations. Although possibly fortuitous, the antisymmetric profiles at $x=4\lambda$ and 6λ are the same shape, with the frequency of the latter twice the frequency of the former. The amplitude of the latter is significantly less than the former, with all of the amplitudes of the antisymmetric profiles less than about 20% of the associated profiles. The antisymmetric profile located at $x=5\lambda$ is not similar to the others.

In the symmetric part of the steepest waveform of Fig. 3, the ratio of the peak-to-peak height of the higher harmonic to the waveform peak-to-peak height is 81%. This same ratio scaled from the limiting case for the $\kappa=1/2$ numerical experiment as given by Schwartz and Vanden-Broeck[2] and shown in their Fig. 3 is 88%. The physical experiment is approaching the limiting case; however, the troughs are not close to bubble encapsulation. This indicates that, perhaps, viscous effects also contribute to the lack of Crapper-like profiles. Additional wavemaker stroke causes the wave field to become three dimensional, and so the notion that three-dimensional instabilities preclude bubble encapsulation is reinforced.

B. The 8.93 Hz experiments

The results of the 8.93 Hz experiments presented in Fig. 4, represent experiments with a noninteger value of n ($=2.5$). That is, this is an example for which there is no Wilton's ripple at exact resonance (i.e., there can be no resonance unless detuning is included in the weakly nonlinear analysis). As is seen from the experiment with the least nonlinearity, the waveform is of the "gravity-type" (i.e., a longer trough and steeper crest). The waveforms shown for the larger wavemaker-stroke steepnesses are either type-2/type-4 or type-5/type-3 depending on the requirement one places on the size of a perturbation which is to be included. For different wave-generation steepnesses, the waveforms measured at the same downstream locations are the same type. As will be seen in the remainder of the experiments, the number of undulations present on the primary wave is the number predicted by the weakly nonlinear theory or that number increased by two. In the cases of the other noninteger n values, 7.94 and 7.25 Hz, the larger adjacent n values are seen to occur. For the 8.93 Hz experiments, both adjacent n values are seen to occur. As with the 9.80 Hz experiments, it is seen that the two (largest) short-wave troughs in the trough of the primary wave are unequal in magnitude with no apparent pattern. The upstream face of the primary wave is less steep than is its downstream face, consistent with the 9.80 Hz experiments.

As the amplitude of the short wave in the trough of the primary wave increases (with increasing ks), the frequency of the short wave apparently does not, nor is its frequency altered as viscosity decreases its amplitude downstream. For the steepest waveform shown, it is seen that there is no inclination of the short-wave troughs with respect to the vertical. The decomposition of the steepest waveform into symmetric and antisymmetric parts shows an interesting feature. At three and five wavelengths downstream, the symmetric parts are similar in shape; however, the shape of the profile at four wavelengths downstream is essentially of type-3 form [as shown in Fig. 1 for the 8.33 Hz ($\kappa=1/3$) waves]. In the 8.33 Hz experiments, it will be seen that waves are of type-3/type-5 form. As 8.93 Hz lies between 9.80 Hz (type-2 profiles) and 8.33 Hz (type-3/type-5 profiles), it is not surprising that both forms appear. The surprising feature is the rapid change in form as there is only one wavelength separating the measurements. The antisymmetric waveforms show a decrease in frequency downstream with a frequency of the fifth, fourth, and third harmonics. Also, the symmetry point with the least mean-square antisymmetric part is within 23% of a temporal

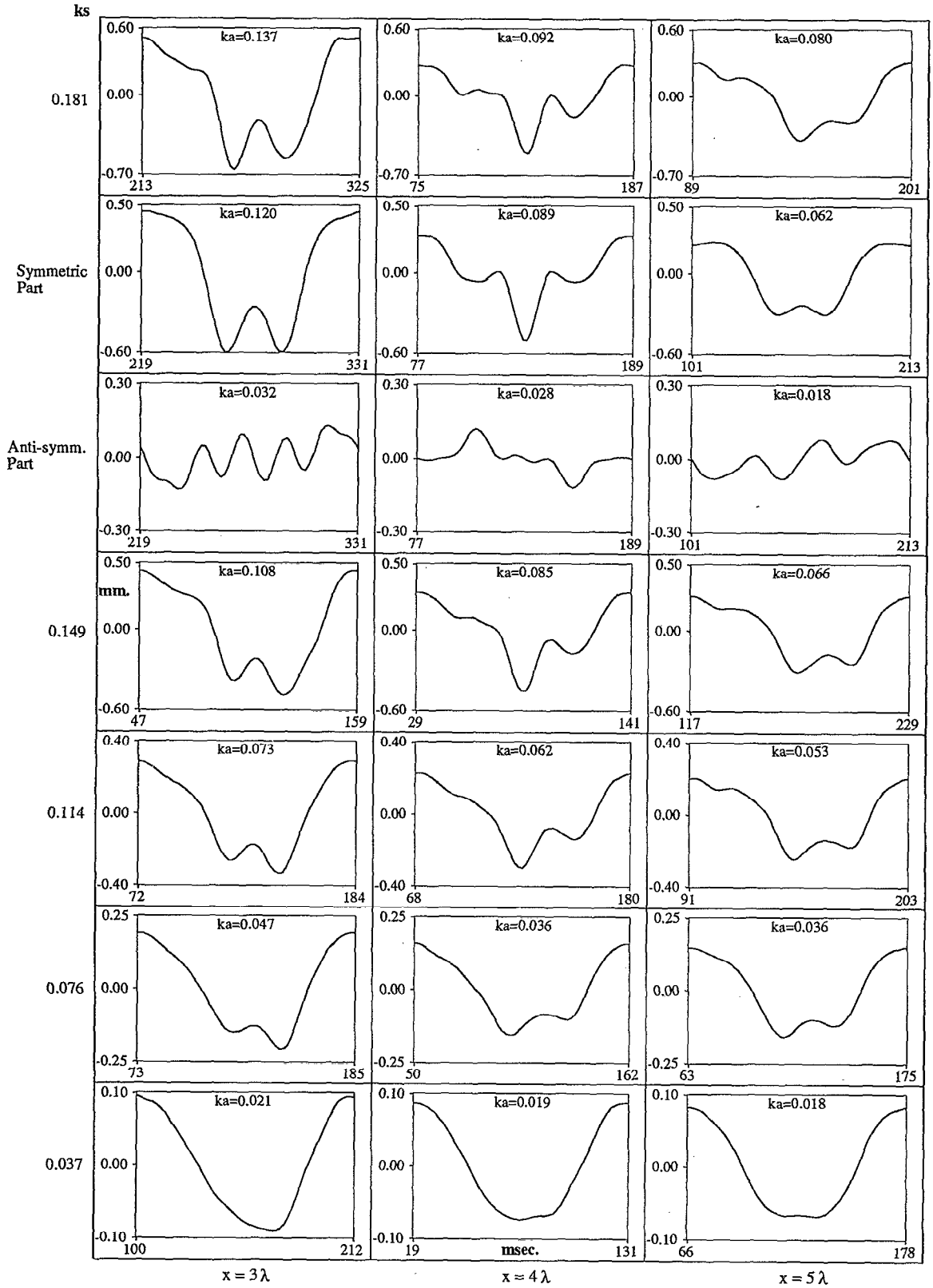

FIG. 4. Wave profiles from the 8.93 Hz experiments are shown for three downstream locations as a function of wavemaker steepness. In addition, the wave profiles from the largest wavemaker steepness are shown decomposed into their symmetric and antisymmetric parts.

period from the midpoint between the global maximum of the waveform, the largest difference in any of the experiments.

C. The 8.33, 7.94, 7.58, 7.25, and 6.94 Hz experiments

Figure 5 presents the experiments for a wavemaker frequency of 8.33 Hz corresponding to $\kappa=1/3$. According to weakly nonlinear theory, this is third-harmonic resonance. Referring to Fig. 1, it is seen that the experimental waveforms shown in Fig. 5 are essentially all of type-5/type-3 form. That is, two large crests are apparent in the trough region of the primary wave and one or three (depending on the magnitude criterion used) in the crest of the primary wave. The primary-wave forms are gravity-type profiles. Also, note that the lowest trough is usually not centered in the waveforms, except when the symmetric part is taken. Asymmetry is present in all of the waveforms and varies downstream, although the form of each wave remains identifiable. An important discovery made by Huh[6] is that gravity-type solutions (type-2 for the 9.80 Hz wave train and type-3 for the 8.33 Hz wave train) are stable when time-marching techniques are used. Unfortunately, each wave type for $\kappa=0.50$ and 0.33 was found to be numerically stable for a sufficiently small wave steepness. The experiments suggest that gravity-type waveforms are stable, which does not violate Huh's findings. Figure 5 shows clearly that as nonlinearity is increased, so is the magnitude of the waves in the trough of the primary wave (i.e., the remnants of the third harmonic). As with the 9.80 and 8.93 Hz experiments, these data show an increase in frequency of the waves in the primary trough as compared to their linear-theory frequencies; however, the frequencies are essentially constant from profile to profile. There is an increase in amplitude of these waves with an increase in *ks*. Also in agreement with the 9.80 and 8.93 Hz data, there are no inclines of the high-frequency troughs with respect to the vertical and the upstream face of the primary wave is less steep than is the downstream face.

The symmetric parts of the waveforms shown in Fig. 5 are consistent with profiles of the type-3 form and are beautifully shaped. The antisymmetric parts show wave trains of approximately uniform frequency and varying amplitude. (The remaining four sets of experiments show the same behavior for the antisymmetric part of the waveforms.) There are five crests and five troughs in each of the antisymmetric profiles which correspond to the type-5 profiles. Other than representing the asymmetry of the measured waveforms, little insight is gleaned from the antisymmetric parts.

In Fig. 6, wave profiles for the 7.94 Hz ($\kappa=1/3.5$) experiments are presented. Profiles are waves of type-6/type-4 form, except for the smallest values. The symmetric-part waveforms, three and four wavelengths downstream, also show a type-6 or a type-4 wave. Five wavelengths downstream, the wave is of type-4 shape. As with the 8.93 Hz experiments, the symmetric part of the profile measured four wavelengths downstream shows a reversal of the short waveform present at the midpoint of the profile. Here, the midpoint position is occupied by a trough at three wavelengths and is occupied by a crest at four wavelengths. Five wavelengths downstream, the symmetric primary-wave trough exhibits neither a high-frequency crest nor a high-frequency trough. The antisymmetric parts show waves with a fourth-harmonic frequency.

Experiments were conducted with 7.58 Hz ($\kappa=1/4$) wavemaker frequencies. (Wave profiles are not presented.) The primary waves were of the gravity-type and exhibit type-6/type-4 forms. Downstream, the waveforms were damped versions of their upstream counterparts. Asymmetry was evident, again. The decompositions of the largest wavemaker-stroke steepness showed type-6 profiles in the symmetric parts and phase-locked "wave trains" with frequencies of the fourth harmonic in the antisymmetric parts.

Also, 7.25 Hz ($\kappa=1/4.5$) experiments were conducted. (Wave profiles are not presented.) These data included the waveform with the largest value of *ka*, 0.288. The profiles exhibited type-7/type-5 shape. Three and four wavelengths downstream, the antisymmetric profiles' frequencies were equivalent to seventh harmonics and had varying amplitude. Five wavelengths downstream, the antisymmetric part's frequency was that of the sixth harmonic. In every experiment, the wave steepness measured five wavelengths downstream exceeded the wave steepness at four wavelengths downstream. This corresponds to a decrease in the amplitude of the short-wave undulations on the primary wave. Apparently, as energy is dissipated by viscosity in the downstream direction, the short-wave energy was damped first; however, the wave steepness actually increases. Although this is seen in other experiments, as already noted, it was most apparent in these experiments.

Surface elevations for the 6.94 Hz ($\kappa=1/5$) experiments are shown in Fig. 7. Type-7 waves are present for the steeper waveforms. An important feature, which is seen in these data, is the rapid (viscous) decay of the short waves. One may argue that this is due to the frequency of these waves. The frequency of the fifth and seventh harmonics are 34.70 and 48.58 Hz, respectively. The actual frequencies measured directly from the data are greater than 42 Hz and so are the highest frequency waves measured. Therefore, it is not surprising that their decay should be the most rapid. On the other hand, the primary wave for this case is the lowest frequency wave investigated and, as such, should exhibit the slowest decay rate. As the computed wave profiles are permanent, nonlinear forms propagating on an inviscid fluid, it is not clear which of these two possibilities is the proper view for the physical experiments. It appears that the former possibility is what occurs. This is in agreement with resonant interaction theory (weakly nonlinear theory) as regards triads with viscosity present (e.g., see Perlin *et al.*[12] for a discussion). The other aspects of the waveforms in Fig. 7 are similar to those already discussed.

In the symmetric part of the steepest waveform of Fig. 7 ($\kappa=1/5$), the ratio of the peak-to-peak height of the short wave centered in the primary-wave trough to the

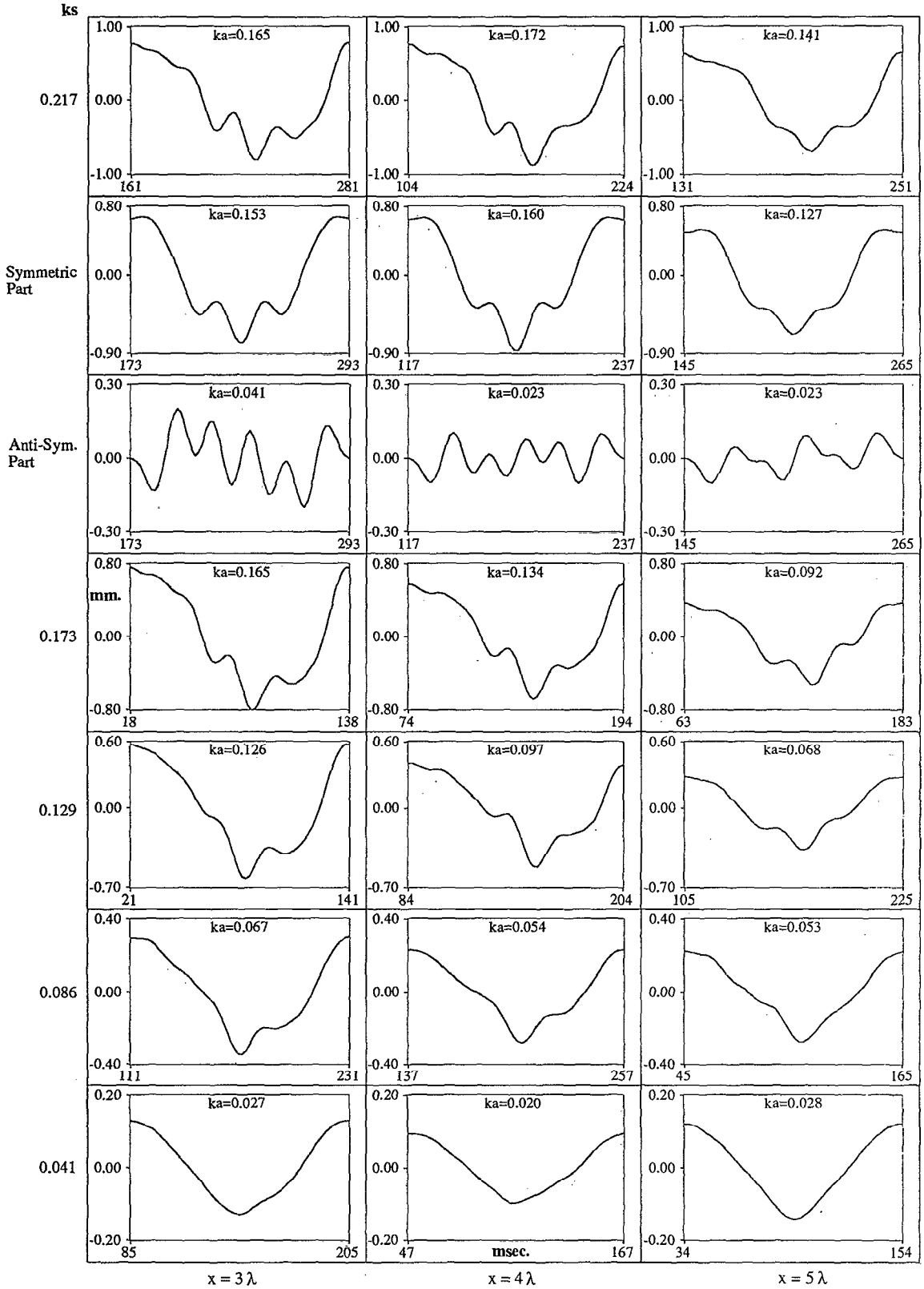

FIG. 5. Wave profiles from the 8.33 Hz experiments are shown for three downstream locations as a function of wavemaker steepness. In addition, the wave profiles from the largest wavemaker steepness are shown decomposed into their symmetric and antisymmetric parts.

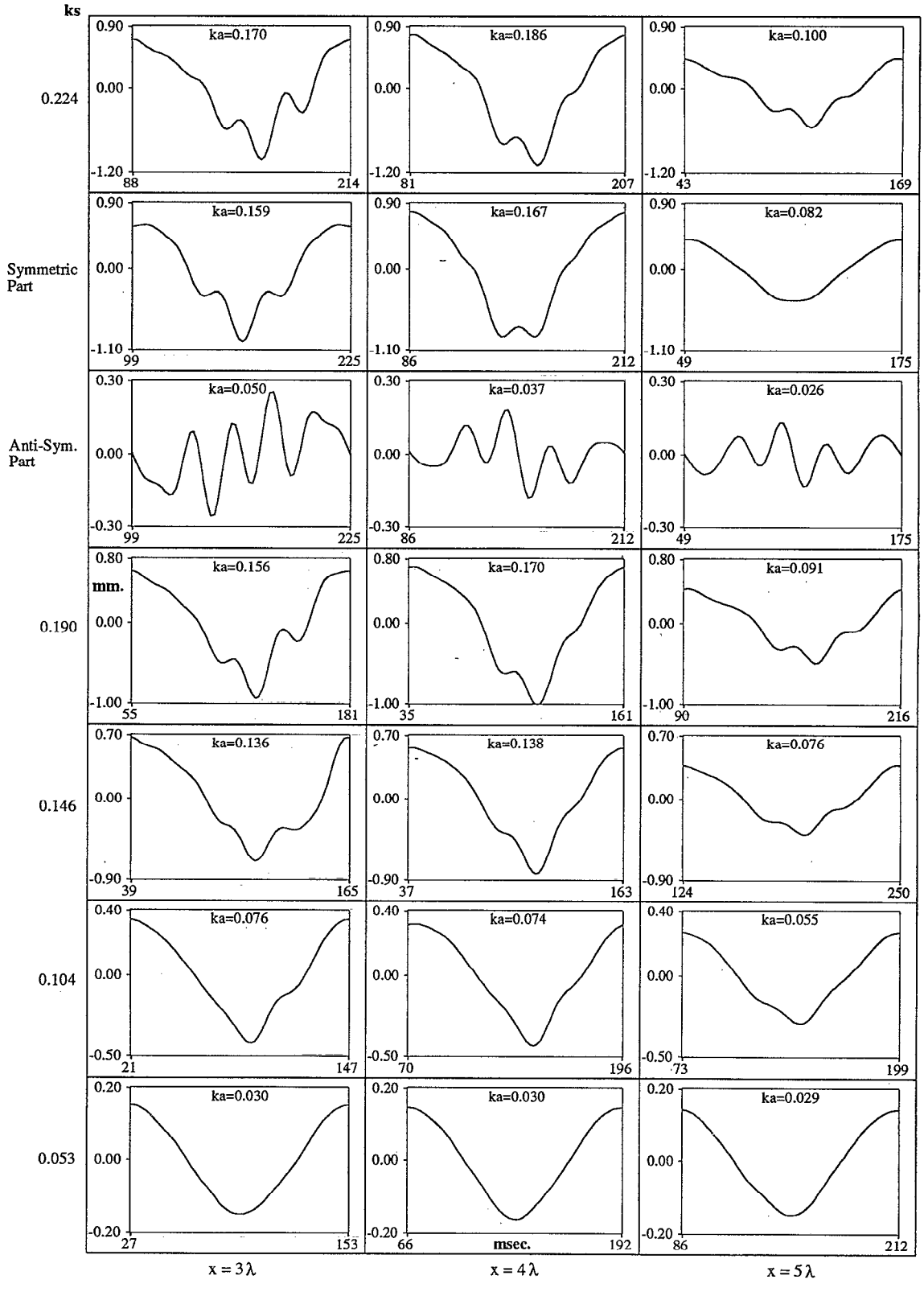

FIG. 6. Wave profiles from the 7.94 Hz experiments are shown for three downstream locations as a function of wavemaker steepness. In addition, the wave profiles from the largest wavemaker steepness are shown decomposed into their symmetric and antisymmetric parts.

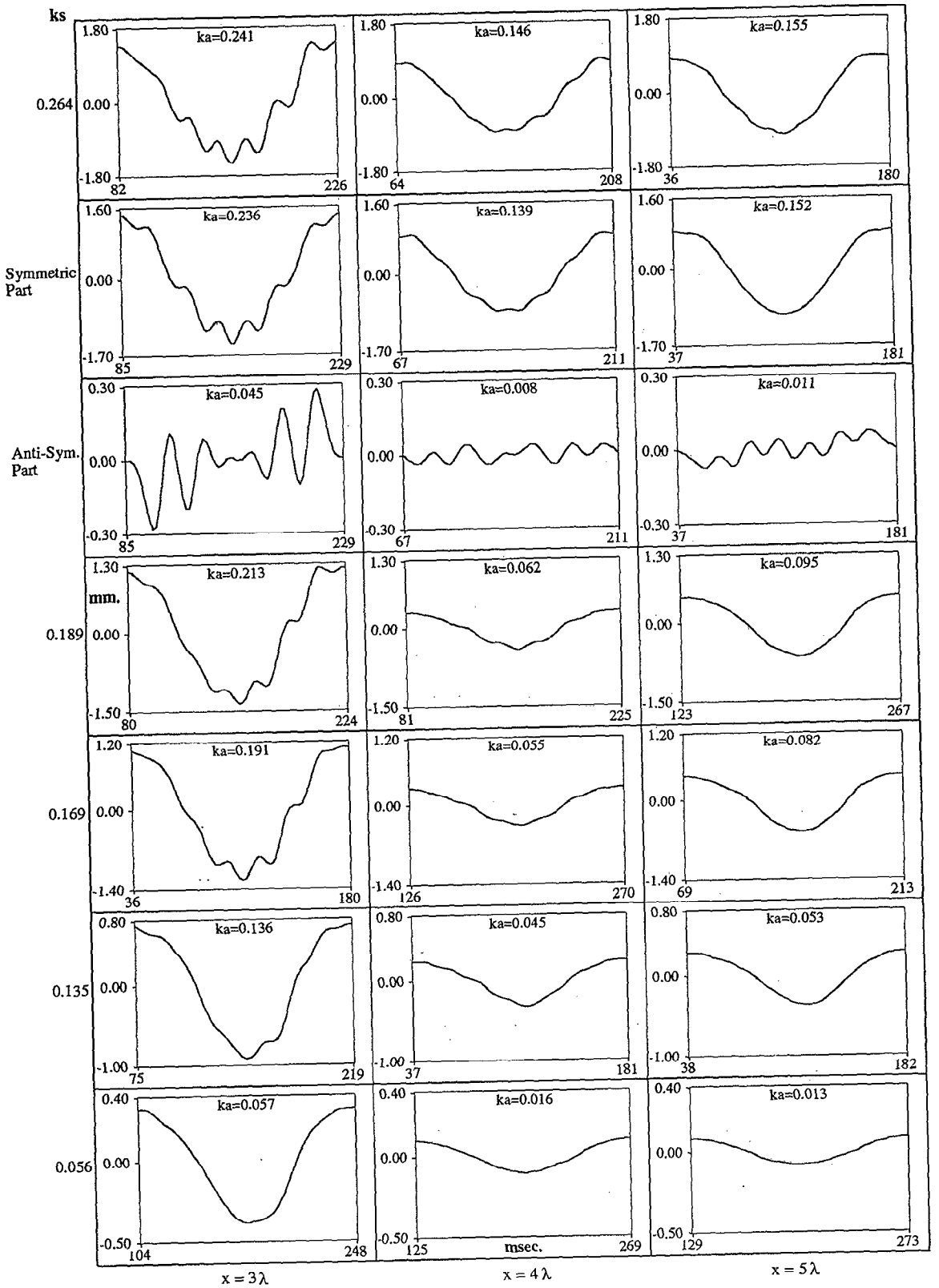

FIG. 7. Wave profiles from the 6.94 Hz experiments are shown for three downstream locations as a function of wavemaker steepness. In addition, the wave profiles from the largest wavemaker steepness are shown decomposed into their symmetric and antisymmetric parts.

profile peak-to-peak height is 19%. This same ratio scaled from the limiting case for the $\kappa=0.19$ as given by Chen and Saffman[4] and shown in Fig. 2 is 40% while for the next steepest profile the ratio is 36%. The physical experiment is not close to the limiting case.

V. CONCLUSIONS

Several important similarities and differences are seen between GC wave computations and measured waveforms which evolve from large, single-frequency sinusoidal oscillations of a paddle that sits astride a uniform-depth channel. All experimental wave profiles are of the gravity-type form with varying degrees of asymmetry. That is, in the absence of the short waves, the primary wave has a broader trough than crest. Therefore, the experimental results (symmetric part) are in general agreement with the results of Schwartz and Vanden-Broeck and Chen and Saffman. In addition, they do not contradict the results of Huh who has investigated numerical stability. Specifying nonsinusoidal analog signals to the wave paddle in an attempt to generate other waveforms, such as those determined numerically, will be a future effort.

Another feature that is seen throughout the experiments is the asymmetry of slope about the crest of the primary waveform. The downstream face of the primary wave exhibits a slope that is steeper than the slope of the upstream face (except in the most nonlinear of the 9.80 Hz experiments). Subsequent experiments using a nonintrusive, optical measurement technique have shown that the steepness difference is present and is not attributable to the disturbance caused by the wave probe.

As the steepness of the waveform increases, there is a steepening of the short waves located in the trough of the primary wave. Also, the crest(s) of the higher harmonic(s) located within the trough region of the primary wave increase(s) with increasing steepness while the trough(s) does (do) the opposite. In the 9.80 Hz experiments, the ratio of peak-to-peak height of the second harmonic to the peak-to-peak height of the waveform attained 92% of the value at which the numerical experiments enclose a bubble, yet the short-wave troughs in the experiments were not closing. As the wavemaker-stroke steepness is increased further, the wave field becomes three dimensional. Thus, the experiments suggest that bubble encapsulation is precluded by three-dimensional instabilities.

The inclination with respect to the vertical of the short-wave trough in the trough of the primary wave as predicted by the numerical solutions is not realized experimentally. It is possible that this inclination is not seen due to the restriction on wavemaker stroke so as to retain a two-dimensional wave field. Experiments on steep, three-dimensional GC wave fields will be a future effort.

Although the amplitudes of the waves in the trough of the primary-frequency wave increase with increasing ks, there are no changes in their frequencies. This is in contradiction to the theory since the wave numbers (as the computations are in the spatial domain) of the undulations increase as do their amplitudes. The disagreement may be due to insufficient steepnesses of the experimental wave trains. Likewise, as viscosity damps the amplitude of the trough waves as they progress downstream, their frequency is unaltered, although they eventually disappear due to viscosity prior to the primary wave disappearance.

As shown in Fig. 7, rapid viscous decay of the undulations in the primary-wave trough of the 6.94 Hz experiments occurs, not the entire waveform decay as is seen in the higher-frequency experiments, Figs. 3–6. As discussed previously, this is in agreement with the resonant interaction theory. That is, although the wave is a nonlinear entity, its viscous decay is consistent with the idea of a superposition of waves of different frequencies, with each wave decaying in a manner consistent with its frequency.

Finally, it is noted that the antisymmetric part of the waveform is difficult to explain. Their steepnesses are approximately 10%–30% of the steepnesses of the symmetric profiles. Except for the 9.80 and 8.93 Hz experiments, the antisymmetric parts of the profile are "wave trains" with varying amplitude and essentially constant frequency for each primary-wave frequency.

ACKNOWLEDGMENTS

We wish to acknowledge and thank William W. Schultz for his detailed comments on the manuscript and for many useful discussions, in general. Also, we appreciate Joe Hammack's comments on the manuscript. We would like to thank the College of Engineering at the University of Michigan for support to construct the Gravity–Capillary Wave Facility.

This research was supported by the Office of Naval Research under an Accelerated Research Initiative, Contract No. N00014-91-J-1083.

[1] M. Perlin and J. Hammack, "Experiments on ripple instabilities. Part 3. Resonant quartets of the Benjamin–Feir type," J. Fluid Mech. **229**, 229 (1991).
[2] L. W. Schwartz and J.-M. Vanden-Broeck, "Numerical solution of the exact equations for capillary–gravity waves," J. Fluid Mech. **95**, 119 (1979).
[3] B. Chen and P. G. Saffman, "Steady gravity–capillary waves on deep water—I. Weakly nonlinear waves," Stud. Appl. Math. **60**, 183 (1979).
[4] B. Chen and P. G. Saffman, "Steady gravity–capillary waves on deep water—II. Numerical results for finite amplitude," Stud. Appl. Math. **62**, 95 (1980).
[5] B. Chen and P. G. Saffman, "Three-dimensional stability and bifurcation of capillary and gravity waves on deep water," Stud. Appl. Math. **72**, 125 (1985).
[6] J. Huh, "A numerical study of capillary–gravity waves," Ph.D. dissertation, Applied Mechanics, University of Michigan, 1991.
[7] A. H. Schooley, "Double, triple, and higher-order dimples in the profiles of wind-generated water waves in the capillary–gravity transition region," J. Geophys. Res. **65**, 4075 (1960).
[8] G. D. Crapper, "An exact solution for progressive capillary waves of arbitrary amplitude," J. Fluid Mech. **2**, 532 (1957).
[9] L. F. McGoldrick, "An experiment on second-order capillary gravity resonant wave interactions," J. Fluid Mech. **40**, 251 (1970).
[10] O. M. Phillips, *The Dynamics of the Upper Ocean* (Cambridge U. P., Cambridge, 1977).
[11] T. B. Benjamin and J. C. Scott, "Gravity–capillary waves with edge constraints," J. Fluid Mech. **92**, 241 (1979).
[12] M. Perlin, D. M. Henderson, and J. Hammack, "Experiments on ripple instabilities. Part 2. Selective amplification of resonant triads," J. Fluid Mech. **219**, 51 (1990).